

Nanoforests composed of ZnO/C core–shell hexagonal nanosheets: fabrication and growth in a sealed thermolysis reactor and optical properties

Muhammad Mohsin Hossain · Hossain Shima ·
Bon-Cheol Ku · Jae Ryang Hahn

Received: 23 April 2014 / Accepted: 26 August 2014 / Published online: 9 September 2014
© Springer Science+Business Media New York 2014

Abstract An efficient method was developed for fabricating a highly porous nanoforest structure composed of ZnO/C core–shell hexagonal nanosheets (HNSs). Compact thermolysis of zinc acetate dihydrate in a sealed bath reactor at 400 °C over 20 h yielded the nanoforest structures. A carbon shell layer coating was applied in situ during the growth of the ZnO nanosheet core. The structures, morphologies, growth processes, compositions, and binding characteristics of the ZnO/C core–shell HNS nanoforests were analyzed using multi-purpose high-performance X-ray diffraction (XRD), scanning electron microscopy, energy-dispersive X-ray spectroscopy, Raman spectroscopy, transmission electron microscopy, and X-ray photoelectron spectroscopy (XPS) techniques. XRD and XPS results suggest the existence of oxygen vacancy defects in the core surface of ZnO/C core–shell. The ZnO/C core–shell HNS nanoforests exhibited strong absorption

features from the visible to the near-IR region (400–1670 nm), and the nanoforest films showed high electrical conductivity.

Introduction

The physicochemical properties of a material vary markedly depending on its structure, morphology, and size [1, 2]. Core–shell nanostructures have attracted significant interest over the past decades because of their tunable surface properties, as well as their enhanced optical, electronic, and catalytic properties. These nanostructures are also potentially useful in a wide range of applications [3, 4], including photoactive materials [5], electron emitters, nanotransistors, electrochemical supercapacitors [6], solar cells [7, 8], transparent conducting oxides, gas sensors, alternative materials for ITOs [9], sophisticated electronic and optoelectronic devices [10], and chemical and biological detectors [8].

ZnO serves as a flexible material in catalysis, piezoelectric transducers, actuators [11], microsensors [12], and photo-electrochemical cells. These applications depend intimately on the nanoscale properties of the ZnO, including the crystal size, orientation, and morphology. Several nanostructured ZnO materials with morphologies such as rods, belts, cables, combs, wires, tetrapods, and hierarchical nanostructures with high degrees of symmetry have been synthesized [9, 13, 14]. ZnO forms polar, hexagonal, highly anisotropic crystals that grow along the *c*-axis, [0001], as a result of the lowest surface energy of the (0002) facet [15]. In addition, the wide band gap (3.37 eV) and large exciton binding energy (60 meV) of ZnO have rendered the material useful in photonic crystals

Electronic supplementary material The online version of this article (doi:10.1007/s10853-014-8569-5) contains supplementary material, which is available to authorized users.

M. M. Hossain · H. Shima · J. R. Hahn (✉)
Department of Chemistry and Bioactive Material Sciences and
Research Institute of Physics and Chemistry, Chonbuk National
University, Jeonju 561-756, Korea
e-mail: jr_hahn@jbnu.ac.kr

M. M. Hossain · B.-C. Ku (✉)
Carbon Convergence Materials Research Center, Institute of
Advanced Composite Materials, Korea Institute of Science and
Technology (KIST), Wanju-gun, Jeollabuk-do, Korea
e-mail: cnt@kist.re.kr

J. R. Hahn
Textile Engineering, Chemistry and Science, North Carolina
State University, 2401 Research Dr, Raleigh, NC 27695-8301,
USA

[16], light-emitting diodes [17], photodetectors [18], gas sensors [19], transparent conducting oxides [9], and optoelectronic devices [20]. The characteristics of ZnO nanomaterials can be further improved by incorporation of carbon. Because carbon works as an electron donor, acceptor, and a hole transport layer, its bonding with ZnO may strongly influence the electronic and optical properties of ZnO. The electrical conductivity of highly crystalline ZnO may be improved by applying a shell layer coating of conductive carbon, which provides several electrochemical advantages [21]. Metal oxide-based composite nanostructures are currently under intensive investigation [22].

Highly porous structures with large surface areas, such as ZnO/C core–shell nanoforests, may be useful in dye-sensitized solar cells (DSSCs) because such structures can absorb large quantities of dyes. This enables the excitation of a greater number of electrons from the valence band to the conduction band, leading to a greater quantity of photoexcited electrons and hence a higher power conversion efficiency. These considerations led us to develop an efficient catalyst-, template-, and solvent-free method for fabricating nanoforests composed of ZnO/C core–shell hexagonal nanosheets (HNSs). The nanoforests were found to form a conductive film on silicon wafers and quartz glass substrates. The solution-phase ZnO/C core–shell HNSs exhibited a strong and broad absorption band from the visible to the near-IR region (400–1670 nm), whereas the pure ZnO film was only UV-active. The novelty of this work stems from the production of highly porous core–shell nanostructures via a simple procedure under easily controlled catalyst-, template-, and solvent-free conditions. The carbon shell layer was deposited in situ onto the surface of the core ZnO nanostructure to improve the electrical conductivity. Potential practical applications of the core–shell nanostructures are discussed.

Materials and methods

Nanoforest of ZnO/C core–shell HNSs

Zinc acetate dihydrate (Sigma Aldrich, 99.999 %, 1.0 g) was placed in a home-built stainless steel reactor ($\sim 30 \text{ cm}^3$ in volume) (SUS 316) sealed with a copper gasket. The reactor was heated in a muffle-type furnace chamber prepared from high-purity fibrous alumina. The temperature was controlled using a programmable silicon-controlled rectifier. HNS nanoforests were fabricated at a temperature of 400 °C over 20 h. After thermolysis, the reactor was slowly cooled to room temperature under programmed control over 4 h to achieve smooth fabrication. The product, a brown solid, was collected and washed in ethanol and then subjected to sonication for 1 min by a low-concentration HCl solution

(0.1 %) to remove the uncoated ZnO. Highly concentrated acid was avoided to protect the carbon-coated ZnO HNSs. Acid was removed from the HNS nanoforest by washing several times in distilled water. Finally, the product was washed with acetone and dried in a vacuum oven for 6 h at 100 °C. The products were characterized using multi-purpose high-performance X-ray diffraction (XRD, X'pert Powder, PANalytical) techniques. Scanning electron microscopy (SEM) images were obtained using a JEOL JSM-6400 microscope under accelerating voltage of 0.2–40, 0.2–5 (in 100 V steps), and 5–40 kV (in 1 kV steps). X-ray energy-dispersive spectroscopy (EDX, Horiba, EMAX) was used in conjunction with FE-SEM (S-4700, Hitachi, Japan) to understand the chemical constituents of the materials. Transmission electron microscopy (TEM) measurements were obtained using a JEOL JEM-2010 microscope, and Raman spectroscopy (HORIBA JOBIN YVON, Lab RAM HR, Laser 514.54) and X-ray photoelectron spectroscopy (XPS, K- α , Thermo Scientific, USA) experiments were conducted to characterize the carbon and oxygen atoms in the ZnO/C core–shell HNS nanoforest film. Absorption property was characterized by UV–Vis near-IR spectroscopy (V670, JASCO, Japan). The electrical conductivity of the film was measured using a four-point probe instrument (FPP, RS8, DasolEng).

The nanoforest film

The HNS nanoforest was dissolved in ethanol under low-power bath sonication over 1 min. The HNS nanoforest solution was then dropped onto a silicon wafer or a quartz glass and dried at 250 °C for 2 h on a hot plate. The electrical conductivity of the film was improved by placing the HNS nanoforest film, which had been prepared on a silicon wafer or a quartz glass put in a glass vial, in a stainless steel reactor containing 0.5 g zinc acetate dihydrate. The film was then heated at 500 °C for 10 or 20 h. Heating the film reduced the as-prepared carbon product, and carbon was further deposited onto the HNSs.

Pure ZnO and residual carbon

Pure ZnO nanoparticles from the ZnO/C core–shell HNS nanoforest were prepared using concentrated HCl [23]. Dissolving the ZnO/C core–shell HNSs in concentrated HCl produced residual carbon (insoluble phase) and ZnCl_2 (solution phase). The residual carbon was filtered and separated from the ZnCl_2 solution. The ZnCl_2 solution was reacted with a 5 % NaOH solution to produce the $\text{Zn}(\text{OH})_2$ precipitate. The precipitated $\text{Zn}(\text{OH})_2$ was collected by filtration and then dried at 70 °C under vacuum for 24 h. During the drying step, pure ZnO nanoparticles were produced from $\text{Zn}(\text{OH})_2$ by dehydration.

Results

ZnO/C core–shell HNS nanoforests

Figure 1 shows the XRD patterns of the as-prepared ZnO/C core–shell HNS nanoforests produced by heating zinc acetate dihydrate at 400 °C for 20 h in a sealed bath. The patterns were collected from samples prior to dilute acid treatment (curve *a*), after complete treatment with HCl (for the insoluble carbon fraction) (curve *b*), and after isolation of the pure ZnO (curve *c*), which was produced after removing the carbon shell from the ZnO/C core–shell HNS nanoforests. All diffraction peaks in curves *a* and *c* were indexed as ZnO (JCPDS No. 01-075-0576) and agreed well with the peaks corresponding to standard wurtzite ZnO (space group: $P63mc$ (186), $a = 0.325$ nm, $c = 0.5207$ nm). The XRD pattern of the insoluble product (residual carbon) upon HCl treatment (curve *b*) was indexed as a low-crystalline carbon. No peaks relating to carbon were observed in curve *a*. The carbon phase could not be detected by XRD, possibly due to the formation of an amorphous carbon shell around the ZnO core. The peak positions of the ZnO/C core–shell (curve *a*) HNSs matched those of pure ZnO nanoparticles (curve *c*), indicating that the strains induced by the amorphous carbon shell were insufficient to change the lattice constants of the ZnO HNS cores; however, the ratios among the intensities of the (100), (002), and (101) diffraction peaks in curve *c* differed somewhat from those obtained from curve *a* (0.76:1:1.31 to 1.50:1:2.43). These results indicated that the pure ZnO precipitates may have been selectively generated with (002) facets. The peak at the (102) plane (marked by an arrow in curve *a*) indicated that non-oxidized free zinc centers were present. This result suggested that oxygen vacancy defects formed in the ZnO/C core–shell HNSs.

The morphology and size of the as-prepared products prior to acid treatment were obtained by SEM imaging, which revealed the growth of the HNS nanoforests (Fig. 2). The SEM images displayed well-aligned and vertically grown HNS nanoforests on the substrates. Figure 2a shows that the HNSs were aligned along the diagonal direction after heating for 17 h at 400 °C. All HNSs appeared to be very similar at this stage. Further heating (to induce growth) for 20 h at 400 °C (Fig. 2b) increased the size of the HNSs, and additional hexagonal HNSs were found in the nanoforest. These images also indicated that the structure between the nanosheets was highly porous.

Figure 3a and b shows the TEM and HR-TEM images of ZnO/C core–shell HNS. The transparent carbon layer was shown by arrow in Fig. 3a. The HR-TEM image shows that the amorphous carbon layer was scattered over the ZnO crystal nanosheets. A ZnO crystalline phase was observed under the carbon layer. The selected area electron

diffraction (SAED) pattern (Fig. 3c) revealed a hexagonal structure indicative of single-crystalline ZnO. A ring pattern with a low intensity was also observed in the SAED pattern, corresponding to the amorphous carbon shell. The EDS analysis of ZnO/C core–shell HNS (Fig. 4a) confirmed that the HNS nanoforests contained Zn, C, and O, consistent with the XRD results (Fig. 1).

Acid treatment of the ZnO/C core–shell nanosheets produced soluble $ZnCl_2$ in the aqueous phase and a carbon precipitate. Figure 3d shows an FE-SEM image of the carbon precipitate, which formed thin sheets. The acid broke down the edge of the carbon shell layer. XRD studies (curve *b* in Fig. 1) of the residual carbon atoms revealed broad peaks corresponding to the (002) and (101) planes at 23.8° and 44.5°, respectively, indicating the presence of an amorphous phase. The EDX spectrum of the residual carbon atoms (Fig. S1) revealed both carbon and oxygen peaks, indicating that the residual carbons may have included oxygen-containing functional groups. The

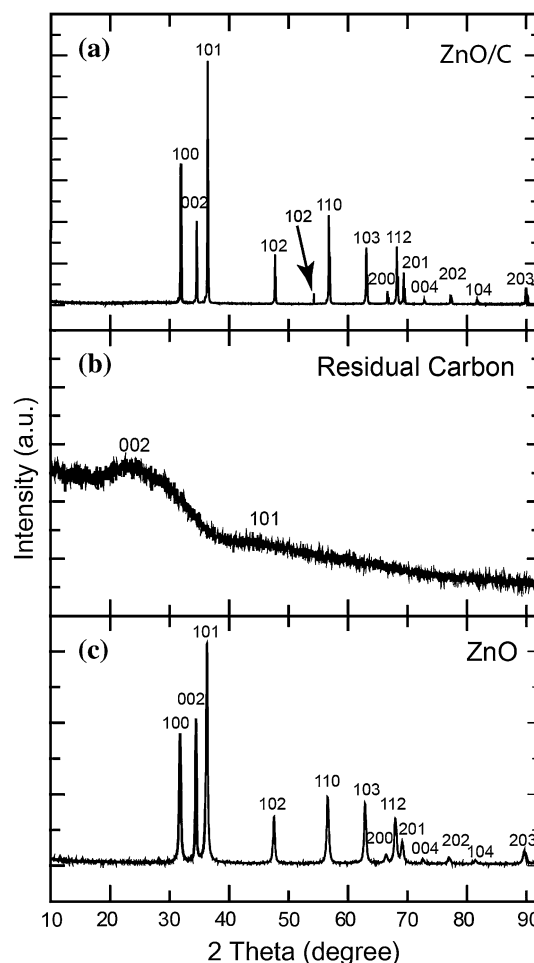


Fig. 1 XRD pattern obtained from curve *a* the ZnO/C core–shell HNS nanoforest, curve *b* the amorphous residual carbon, and curve *c* the pure ZnO nanoparticles

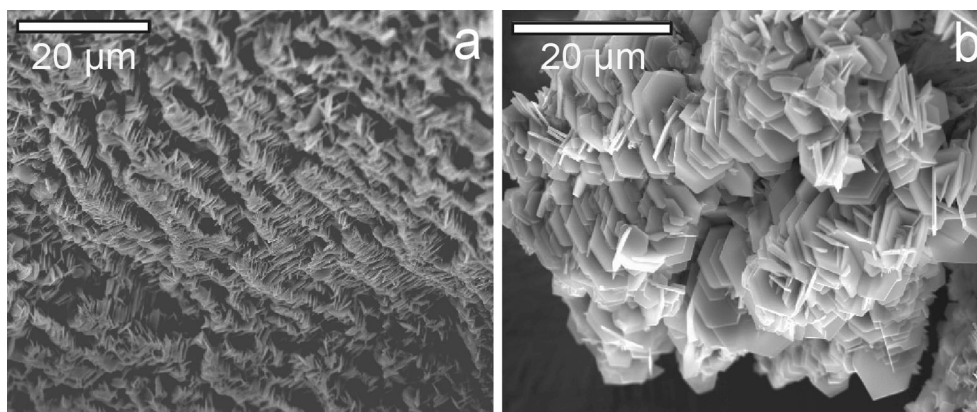


Fig. 2 SEM images of ZnO/C core-shell HNS nanoforests grown at 400 °C for **a** 17 h and **b** 20 h

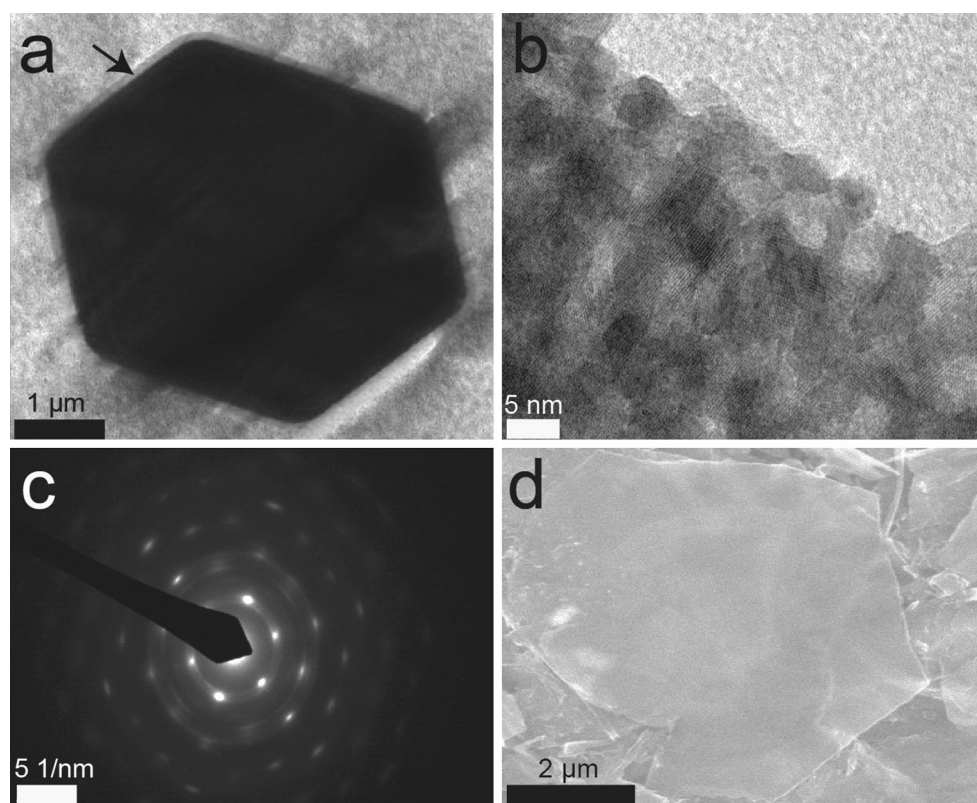


Fig. 3 **a** TEM image of ZnO/C core-shell HNS, **b** HR-TEM images of ZnO/C core-shell HNS, **c** SAED patterns of the ZnO/C core-shell HNSs, and **d** FE-SEM image of residual carbon layer isolated from ZnO/C core-shell nanosheets by acid washing

presence of the oxygen-containing functional groups increased the *d*-spacings between the carbon shell layers, producing an amorphous feature and a broad band in the XRD peaks (curve *b* in Fig. 1).

The ZnO/C core-shell HNS nanoforest growth process at 400 °C was explored by conducting reactions over different periods of time at a given temperature. SEM images collected after each period are shown in Figs. 5 and S2. Rod-like shape of ZnO/C begins to appear after heating for

5 h (Fig. S2a). After heating for 10 h, rods with a tower shape were formed (Fig. 5a). Additional heating (12 h) induced the growth of a few sheets from the rods (Fig. 5b). The number of sheets increased over 14 h (Fig. 5c). The tower-shaped rods finally split into nanosheets after 15 h of heating (Fig. 5d). A nanoforest was produced after 17 h of heating (Fig. 5e, f). The nanosheets were found to be stacked along the towers. The HNS composed of nanoforests was found to be further developed in size and shape

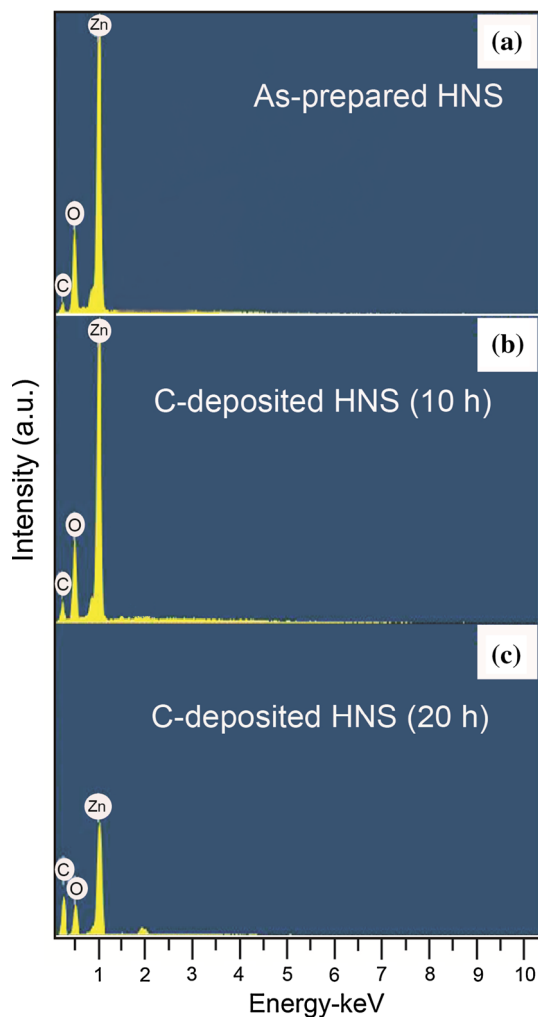


Fig. 4 EDX spectra of **a** an as-prepared ZnO/C core-shell HNS nanoforest film grown on a silicon substrate at 400 °C for 20 h, and a ZnO/C core-shell HNS nanoforest film further heated at 500 °C for **b** 10 h and **c** 20 h using zinc acetate dihydrate as a carbon source in a sealed bath for the deposition of additional carbon atoms onto the shell layer

after 18 h of heating (Fig. 5g) and was complete by 20 h of heating (Fig. 5h). Further heating over 25 h produced a similar feature to Fig. 5h (Fig. S2b).

The SEM images recorded throughout the formation of the ZnO/C core-shell HNS nanoforests were used to prepare a schematic diagram of the nanoforest growth process, as shown in Fig. 6. Microparticles of zinc acetate dihydrate (Fig. 6a) grew into the ZnO/C core-shell rod structure after 10 h of heating (Fig. 6b). Further heating multiplied the rods (Fig. 6c). After multiplication, the rods began to split into HNSs (Fig. 6d–g). The tip parts (angles) formed and hexagonal shapes developed from the rods. The sizes of the hexagonal shapes grew over 20 h of heating.

A ZnO/C core-shell HNS nanoforest could be synthesized as follows. Water molecules in the $Zn(CH_3COO)_2 \cdot 2H_2O$ structure were removed as the temperature was

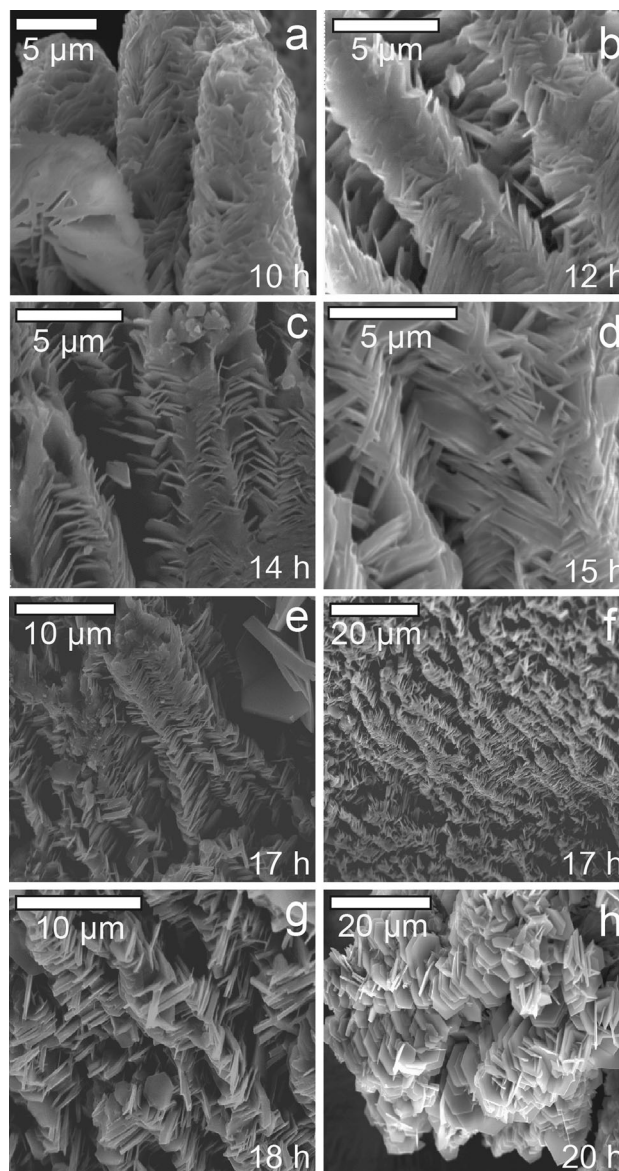
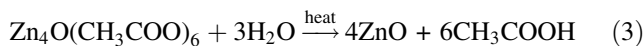
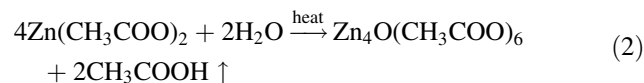
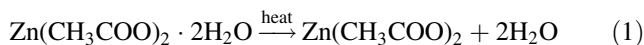


Fig. 5 SEM images obtained during the growth of the ZnO/C core-shell HNS nanoforests at 400 °C as a function of time. **a** Tower-like rods formed upon heating over 10 h. **b** Sheets grew from the rod-like towers over 12 h. **c** The number of sheets that formed increased after 14 h. **d** The rods split into nanosheets at 15 h. **e, f** Nanosheets that resembled a forest formed after 17 h. **e** shows a magnified image obtained from **f**. **g** The sizes and shapes of the nanosheets developed further up to 18 h. **h** Complete growth of the HNS nanoforest was achieved after 20 h

increased (Reaction 1). The structures then decomposed to yield ZnO, carbon, and hydrocarbon, as shown below [24]:



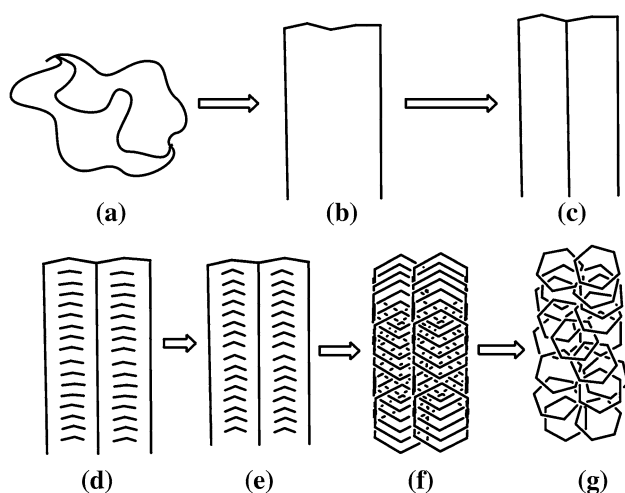
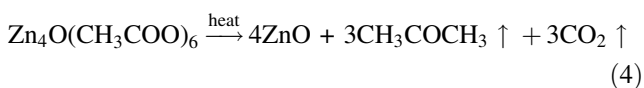


Fig. 6 Schematic diagram showing the HNS nanoforest growth process at 400 °C. **a** ZnO microparticle structure obtained after growth for less than 10 h. **b** The rod structure formed from the particles. **c** The rod was split into two rods. **d** The tips of the nanosheets grew along the rod. **e** The angle of the tip sharpened to form HNSs. **f** HNSs developed. **g** Complete formation of the HNS nanoforest after 20 h



ZnO formed polar, hexagonal, highly anisotropic crystals that grew along the *c*-axis [0001] due to the low surface energy of the [0002] facet [25]. The thermodynamic properties of the structure may enable the formation of the hexagonal shape. The ZnO/C core-shell structure was formed by the deposition of carbon onto the ZnO surfaces. The hydrocarbons were vaporized and burned, and ZnO nanoparticles were produced by the reactions (3) and (4). During the decomposition of the Zn organic compounds to yield ZnO and hydrocarbons, burning hydrocarbons could be deposited onto the ZnO in a sealed reaction system.

A comprehensive analysis of magnified images of several HNSs after different heating times revealed that the HNSs split during the reaction, as shown in Fig. 7. Figure 7a shows a thick HNS that could be split into two or several thinner HNSs, as shown in Fig. 7b and c. The splitting continued more and more, such that the HNS thickness decreased (Fig. 7d, e). Figure 7f shows a completely split HNS structure in a nanoforest. Close inspection of several splitting processes led us to propose the schematic growth process shown in Fig. 8. The first splitting event occurred at position 1 of the HNS (Fig. 8a–d). The second splitting event occurred at position 2, as shown in Fig. 8e–g. Further subsequent splitting events at positions 6, 5, and 3 completed the splitting of the single HNSs into two HNSs (Fig. 8h–l). The number of angles in a nanosheet increased with the successive splits at each position.

Effects of the carbon shell on the electrical conductivity and absorption properties

We fabricated films composed of ZnO/C core-shell HNS nanoforests on quartz and Si substrates and measured the electrical conductivities of the structures. SEM images of the nanoforest films grown on quartz and Si substrates (Fig. 9a, b, respectively) revealed that the films retained the porous structure of the HNS nanoforests. The conductivity of the as-prepared ZnO/C core-shell HNSs was $1.5 \times 10^{-4} \text{ S m}^{-1}$. This conductivity was improved to 35 S m^{-1} by applying a further coating of carbon onto the shell layer of the HNSs. Additional carbon atoms were deposited by placing the ZnO/C core-shell HNS films in a glass vial, which was then placed in a stainless steel reactor containing zinc acetate dihydrate as a carbon source. Heating to 500 °C for several hours resulted in the deposition of carbon onto the HNS nanoforests. SEM images after carbon deposition revealed that the same HNS nanoforest structures were preserved (Fig. S3) with a high porosity.

The deposition of a carbon coating on the shell of the ZnO/C core-shell HNSs was confirmed by EDX and Raman spectroscopy analyses. Figure 4b and c shows the EDX peaks of the ZnO/C core-shell HNS films heated at 500 °C for 10 and 20 h in the presence of a carbon source, respectively. The carbon fraction increased relative to the as-prepared products (Fig. 4a). Raman spectroscopy revealed the characteristics of the carbon shell after coating (Fig. 10). Curve *a* shows that the intensities of the D and G bands of the coated carbon shell were higher than those of the as-prepared HNSs (curve *b*). The Raman spectrum of a pure ZnO film (curve *c*) did not display D and G bands. The presence of a high-intensity D band (curve *b*) relative to the G band indicated that the HNS core-shell materials included defects or amorphous carbon atoms. The defect carbon atoms may have been reduced by restoring the double bonds in defects upon heating at 500 °C. The relative increase in the G band (curve *a*), compared to the D band intensity, after carbon coating at 500 °C, suggested that the reduction was carried out. Restoring the double bonds provided an extended conductive path that should improve the electrical conductivity of the material. A greater quantity of carbon was found to have been deposited during the decomposition of zinc acetate upon heating in a sealed bath. Further deposition of the carbon layer on the surface of the ZnO/C core-shell, as well as the reduction of carbon, may improve the electrical conductivity. The electrical conductivity increased from 1.5×10^{-4} to 35 S m^{-1} , which was comparable to the values obtained from other carbon composite materials [26–28]. The peaks around 433 cm^{-1} (Fig. 10a–c) and 576 cm^{-1} (Fig. 10b, c) were attributed to the E_2 (high)

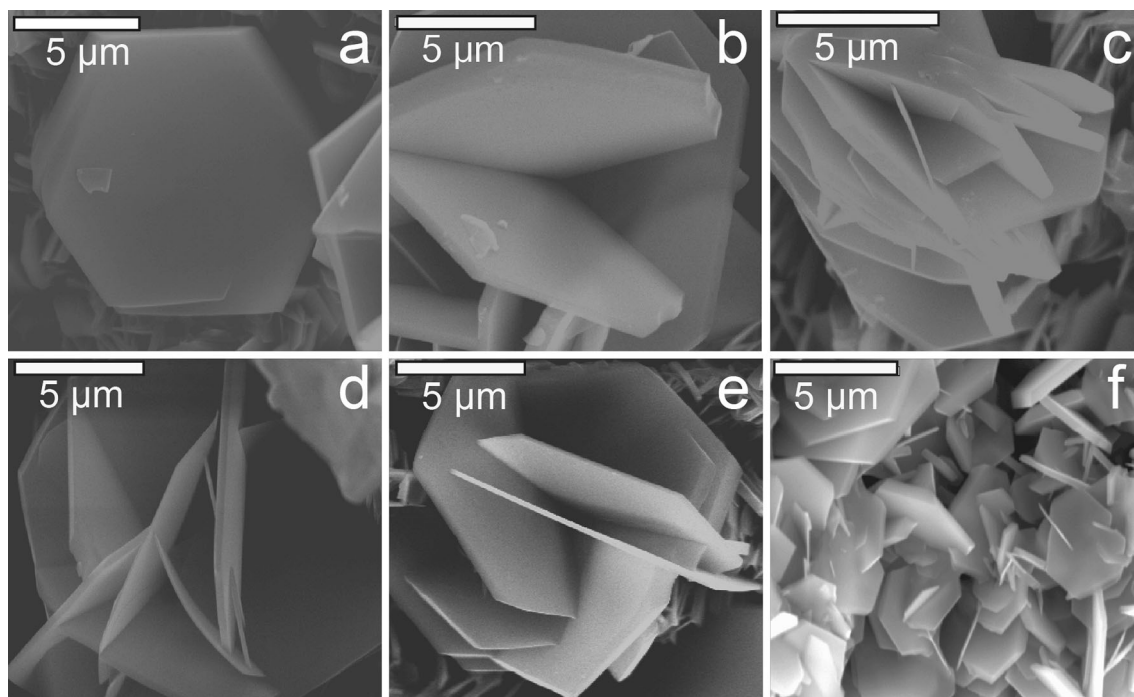


Fig. 7 SEM images showing the splitting of the HNSs. **a** A thick HNS. **b–d** HNS splitting. **e** The last stage of HNS splitting. **f** Completion of the HNS splitting process in the nanoforest

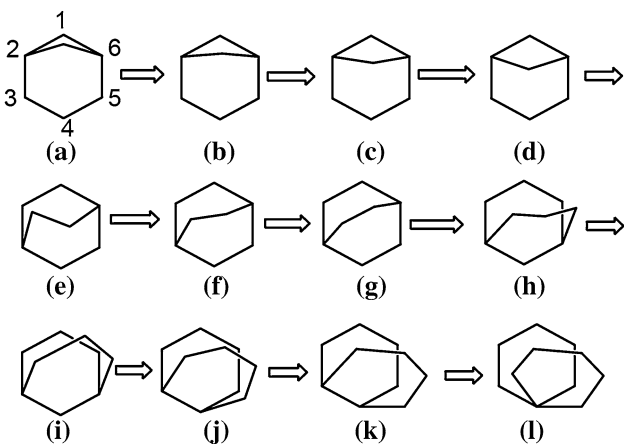


Fig. 8 Schematic diagram showing the splitting of HNSs. **a–d** Formation of the first HNS angle at position 1. **e–g** Half of the HNS grew through the formation of a second angle at position 2. **h, i** Growth of a third HNS angle at position 6. **j, k** Growth of a fourth HNS angle at position 5. **l** Growth of fifth and sixth HNS angles at positions 3 and 4

phonon frequency [29] and the A1-LO phonon mode [30] of the ZnO nanocrystal, respectively, as confirmed by the spectrum of the pure ZnO film (curve *c*). The A1-LO phonon mode intensity was reduced in the carbon-coated ZnO/C core-shell species, possibly due to the long heating time.

The binding characteristics of the carbon layer on the ZnO core were characterized by investigating the carbon-coated ZnO/C core-shell HNSs by XPS analysis. The $2p_{3/2}$

and $2p_{1/2}$ peaks (curve *a* in Fig. 11) at 1022.0 and 1045 eV, respectively, were attributed to ZnO. The O1s peak (curve *b*) was deconvoluted into three components located at 531.66, 532.48, and 533.01 eV. The low-energy peak at 531.66 eV corresponded to the O^{-2} species in the wurtzite structure of the ZnO lattice, and the peak at 532.48 eV corresponded to the C=O groups bonded to Zn in the poorly crystalline carbon shell layer [31]. The high-energy peak (533.01 eV) originated from the C–O functional group [32]. The energies of the deconvoluted peaks of O1s were slightly higher, possibly due to the incorporation of the more electronegative carbon atoms (compared to Zn). Here, the peaks corresponding to the C=O and C–O groups in the ZnO species indicated that Zn was chemically bonded to C=O or C–O at the interface between the ZnO sheets and the carbon shell layer in the ZnO/C core-shell HNSs. The C1s peak (curve *c*) could be deconvoluted into several components with binding energies of 284.6, 284.8, 285.8, 287.65, and 289.3 eV. These energies were attributed to the C=C bonds in sp^2 carbon atoms, the C–C bonds in sp^3 carbon atoms, C–OH, C=O, and O–(C=O) groups, respectively [33]. The peak at 290.6 eV corresponded to the $\pi-\pi^*$ transition of the sp^2 C=C network in the shell layer. The presence of oxygen-containing functional groups (curve *c*) was consistent with the peaks of the CO group (532.48 and 533.01 eV) in curve *b*.

The XPS analysis revealed carbon, oxygen, and Zn atomic ratios of 36.85, 36.15, and 25 %, respectively. The

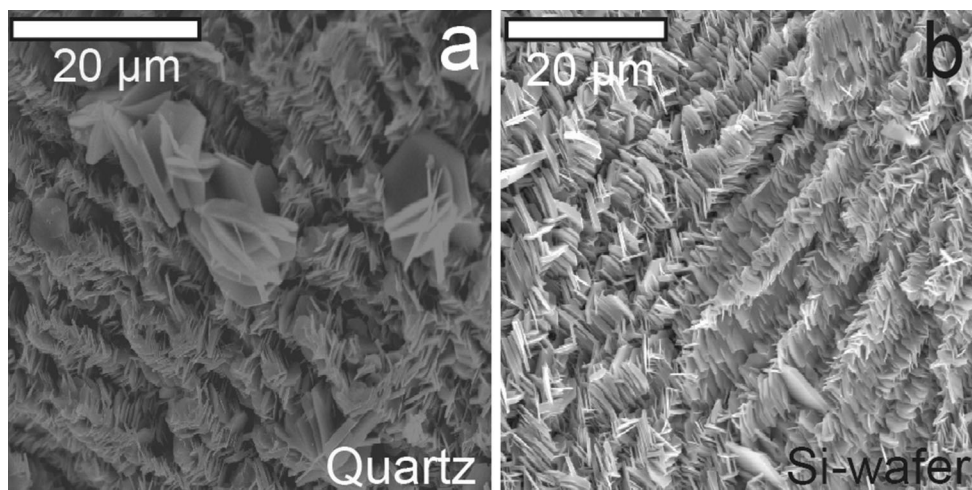


Fig. 9 SEM images of a ZnO/C core-shell HNS nanoforest film **a** prepared on a quartz substrate or **b** on a Si substrate

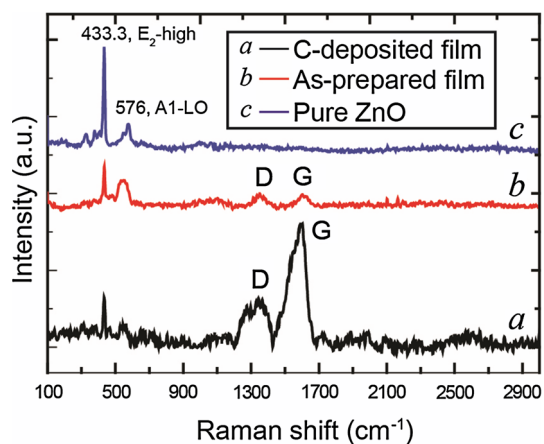


Fig. 10 Raman spectra (curve *a*) of the HNS nanoforest film after deposition of additional carbon atoms at 500 °C over 20 h, (curve *b*) of the as-prepared ZnO/C core-shell HNS nanoforest film grown at 400 °C over 20 h, and (curve *c*) of the pure ZnO film

excess oxygen atoms relative to Zn were attributed to the functional groups in the carbon shell layers (curve *c*). These results were consistent with the Raman, EDX, and XRD measurements: The D band in the Raman spectrum (Fig. 10) indicated the presence of oxygen-containing functional groups, the EDX curve (Fig. S1) included both carbon and oxygen peaks, and the XRD peak at 54° (the 102 plane, Fig. 1a) indicated the presence of free zinc in the core of the ZnO/C core-shell nanosheets. These observations suggested that the core in the ZnO/C core-shell HNSs lacked oxygen atoms and the carbon shell layer included oxygen-containing functional groups. At the interface between the core sheets and shell layers, zincs could form bonds to the oxygen atoms in oxygen-containing functional groups. These binding characteristics yielded an electrical conductivity that was more than a factor of 10^5 times the conductivity obtained from the

as-prepared ZnO/C products. This combination of oxygen-rich carbon shell layers and oxygen-deficient core sheets could play an important role in light absorption.

Discussion

The high porosity and high electrical conductivity of the ZnO/C core-shell HNS nanoforests suggested that these materials may be suitable for use in DSSC applications, gas sensors, and supercapacitors. The applicability of the nanoforests to DSSC, nanocrystal photovoltaic device, and white light photocatalyst applications was investigated by measuring the absorption spectroscopy of the solution-phase ZnO/C core-shell HNS nanoforests (Fig. 12). Solution-phase ZnO/C core-shell HNS was produced by dissolving the core-shell HNS nanoforests in *N*-methyl-2-pyrrolidone, followed by sonication for 25 min. Three different solution concentrations (0.02, 0.05, and 0.1 mg mL⁻¹) were tested. The solution-phase pure ZnO nanomaterials were characterized in an effort to understand the effects of the carbon shell layer on the light absorption properties. A pure ZnO solution (0.05 mg mL⁻¹) was prepared by separating the carbon shell from the ZnO/C core-shell HNS in an acid treatment step. Curve *a* shows the absorption spectrum obtained from the pure ZnO solution (0.05 mg mL⁻¹), which exhibited a strong peak in the UV region and smaller absorption band in the visible region. A solution containing ZnO/C core-shell HNSs at the same concentration displayed a dramatic improvement in the visible absorption bandwidth (curve *c*) (400–1670 nm). A higher concentration, 0.1 mg mL⁻¹, of the ZnO/C core-shell HNSs displayed the strongest white light absorption behavior (curve *d*). Furthermore, the lower concentration solution (0.02 mg mL⁻¹) displayed greater

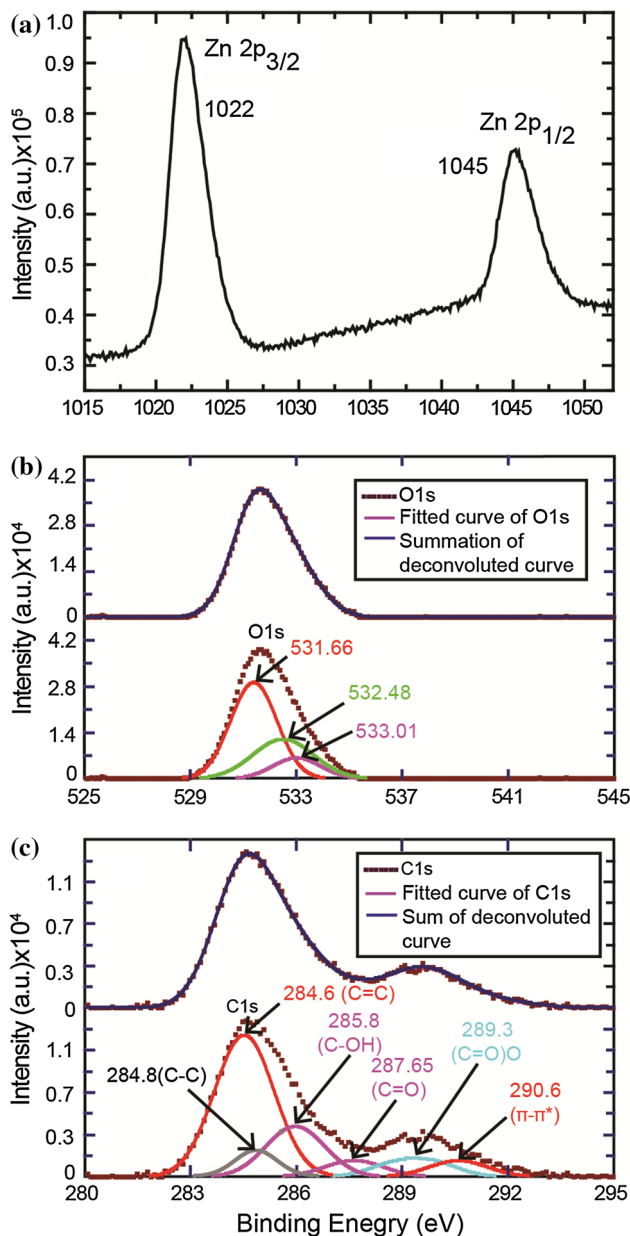


Fig. 11 XPS spectra of **a** Zn 2p, **b** O1s, and **c** C1s core level of ZnO/C nanosheet materials

light absorption in the visible to near-IR region (curve *b*) compared to the pure ZnO solution (0.05 mg mL⁻¹). These results indicated that the presence of a carbon shell in the ZnO/C core-shell HNSs increased the absorption profile across the visible and near-IR regions, as well as increasing the electrical conductivity.

Absorption at longer wavelengths may be related to Zn defect centers (*d-d* transition) [34]. As the ZnO/C core-shell concentration in the solution was increased, the absorption peak intensity increased across the full visible–near-IR spectrum, although the UV peak was shifted toward shorter wavelengths relative to the peaks obtained

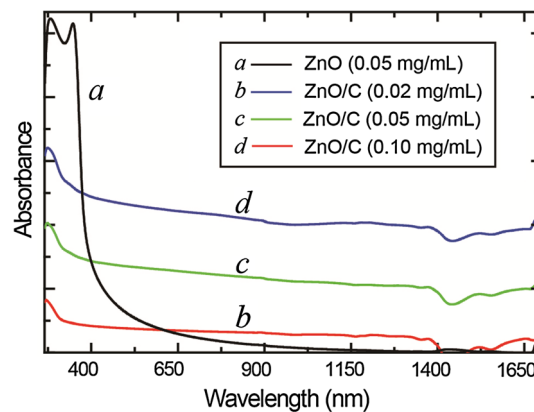


Fig. 12 UV–Vis–near-IR spectra of a nanoforest composed of pure ZnO (curve *a*) and ZnO/C core-shells HNS (curves *b–d*) prepared at different concentrations

from the pure ZnO sample, possibly due to surface plasmon excitation [35–37]. This suggested that the absorption intensity could increase upon further carbon deposition. Further carbon deposition on the ZnO/C core-shell HNSs eventually increased the thickness values of the nanosheet. Therefore, the absorption band broadened and the absorption peak was shifted toward shorter wavelengths (Fig. 12b–d). The light absorption properties could be enhanced through multiple light scattering effects due to the gaps in the nanoforest nanosheets [38, 39]. Light could be trapped more readily by scattering it in multiple directions between the gaps of the nanosheets.

The carbon coating layer improved the electrical conductivity and the light absorption efficiency of the ZnO nanosheets, as well as the stability of the ZnO nanostructures in DSSCs. In a DSSC, ZnO nanoparticles react with the carboxylic groups of acidic dye molecules during immersion of the nanoparticles in the acidic dye solution. The reaction eventually forms Zn²⁺/dye agglomerate complexes [40] on the surfaces of the ZnO nanoparticles. These effects consequently decrease the adsorption of dye molecules onto the nanoparticle surfaces, and the agglomerated dye complexes become incapable of electron injection into the photoanode. The overall power conversion efficiency of the DSSC devices, therefore, decreased. The formation of a Zn²⁺/dye agglomerate complex may be prevented by using shell materials composed of TiO₂ or SiO₂ to improve the stability of the ZnO nanoparticles in the acidic dye. The coated ZnO nanoparticles displayed an enhanced stability and higher power conversion efficiency [41]. The presence of the Al₂O₃ shell layer improved the stability of the ZnO nanoparticles and also functioned as an insulator [42] on the ZnO surfaces. This insulating layer resisted photoexcited electron injection from the conduction band of the photosensitizer dye into the semiconductor

photoanode. As a result, the overall device efficiency decreased. High-efficiency DSSC fabrication, therefore, requires the use of a conductive and stable shell layer. In this context, the conductive stable carbon shell layer of a ZnO/C core-shell HNS could pave the way for the development of promising materials for use in DSSCs. As a white light photocatalyst, several characteristics including visible light absorption, high electrical conductivity (to reduce recombination), well dispersibility, dye degradation efficiency, and recycle performance are required. It is possible that the HNS nanoforest may have the less photo-corrosion because of the stable carbon shell layer, which can be favorable for the recycle performance. The strong light absorption profile across the visible and near-IR regions, the high electrical conductivity, and the good stability of the carbon shell in the ZnO/C core-shell HNSs highlight the potential utility of these structures in nanocrystal photovoltaic devices, white light photocatalytic applications, and white light emitters.

Conclusions

Highly porous and conductive ZnO/C core-shell HNS nanoforests were fabricated through the direct decomposition of zinc acetate dihydrate in a sealed thermolysis stainless steel vessel at 400 °C without using a catalyst, solvent, or template. The carbon shell layer coating was applied in situ during the growth of the ZnO nanosheet core. The thickness of the carbon shell layer increased, thereby enhancing the electrical conductivity of the ZnO/C core-shell materials. The HNS growth process was monitored and electrically conductive ZnO/C core-shell HNS nanoforest films were fabricated. Finally, the ZnO/C core-shell HNS nanoforests exhibited strong absorption features in the visible and near-IR regions (400–1670 nm), indicating the practical utility of the materials in DSSCs, nanocrystal photovoltaic devices, white light emitters, and white light photocatalyst applications. These properties may potentially be improved with the addition of a carbon shell layer.

Acknowledgements This work was supported by grants from the Korean government (NRF, MSIP, 2010-0024254 and 2007-0056095), and HS and MMH were supported by the BK21 PLUS program. In addition, Dr. B-C. Ku was supported by a grant from KIST institutional program (2Z04250).

References

- Xai Y, Yang P, Sun Y, Wu Y, Mayers B, Gates B, Yin Y, Kim F, Yan H (2003) One-dimensional nanostructures: synthesis, characterization, and applications. *Adv Mater* 15:353–389
- Xei X, Li Y, Liu ZQ, Haruta M, Shen W (2009) Low-temperature oxidation of CO catalysed by Co_3O_4 nanorods. *Nature* 458:746–749
- Qian HS, Yu SH, Luo LB, Gong JY, Fei LF, Liu XM (2006) Synthesis of uniform te@carbon-rich composite nanocables with photoluminescence properties and carbonaceous nanofibers by the hydrothermal carbonization of glucose. *Chem Mater* 18:2102–2108
- Caruso F (2001) Nanoengineering of particle surfaces. *Adv Mater* 13:11–22
- Jiang L, Gao L (2005) Fabrication and characterization of ZnO-coated multi-walled carbon nanotubes with enhanced photocatalytic activity. *Mater Chem Phys* 91:313–316
- Kalpana D, Omkumar KS, Kumar SS, Renganathan NG (2006) A novel high power symmetric ZnO/carbon aerogel composite electrode for electrochemical supercapacitor. *Electrochim Acta* 52:1309–1315
- Greene LE, Law M, Tan DH, Montano M, Goldberger J, Somorjai G, Yang P (2005) General route to vertical ZnO nanowire arrays using textured ZnO seeds. *Nano Lett* 5:1231–1236
- Zhang Y, Wang L, Liu X, Yan Y, Chen Ch, Zhu J (2005) Synthesis of nano/micro zinc oxide rods and arrays by thermal evaporation approach on cylindrical shape substrate. *J Phys Chem B* 109:13091–13093
- Pan ZW, Dai ZR, Wang ZL (2001) Nanobelts of semiconducting oxides. *Science* 291:1947–1949
- Pan Z, Budai JD, Dai ZR, Liu W, Paranthaman MP, Sheng Dai S (2009) Zinc oxide microtowers by vapor phase homo epitaxial regrowth. *Adv Mater* 21:890–896
- Martin PM, Good MS, Johnston JW, Bond LJ, Crawford SL (2000) Piezoelectric films for 100-MHz ultrasonic transducers. *Thin Solid Films* 379:253–258
- Xu JQ, Pan QY, Shun YA, Tian ZZ (2000) Grain size control and gas sensing properties of ZnO gas sensor. *Sens Actuators B* 66:277–279
- Huang MH, Mao S, Feick H, Yan H, Wu YY, Kind H, Weber E, Russo R, Yang PD (2001) Room-temperature ultraviolet nanowire nanolasers. *Science* 292:1897–1899
- Dai Y, Zhang Y, Li QK, Nan CW (2002) Synthesis and optical properties of tetrapod-like zinc oxide nanorods. *Chem Phys Lett* 358:83–86
- Li WJ, Shi EW, Zhong WZ, Yin ZW (1999) Growth mechanism and growth habit of oxide crystals. *J Cryst Growth* 203:186–196
- Chen Y, Bagnall D, Yao T (2000) ZnO as a novel photonic material for the UV region. *Mater Sci Eng B* 75:190–198
- Saito N, Haneda H, Sekiguchi T, Ohashi N, Sakaguchi I, Kumamoto K (2002) Low-temperature fabrication of light-emitting zinc oxide micropatterns using self-assembled monolayers. *Adv Mater* 14:418–421
- Liang S, Sheng H, Liu Y, Hio Z, Lu Y, Shen H (2001) ZnO Schottky ultraviolet photodetectors. *J Cryst Growth* 225:110–113
- Lin Y, Zhang Z, Tang Z, Yuan F, Li J (1999) Characterization of ZnO-based varistors prepared from nanometer precursor powders. *Adv Mater* 9:205–209
- Zhang H, Yang D, Ma X, Yujie Ji, Xu J, Que D (2004) Synthesis of flower-like ZnO nanostructures by an organic-free hydrothermal process. *Nanotechnology* 15:622–626
- Liu J, Li Y, Ding R, Jiang J, Hu Y, Ji X, Chi Q, Zhu Z, Huang X (2009) Carbon/ZnO nanorod array electrode with significantly improved lithium storage capability. *J Phys Chem C* 113:5336–5339
- Ding R, Liu J, Jiang J, Li Y, Hu Y, Ji X, Chi Q, Wu F, Huang X (2009) High surface area ZnO-carbon composite tubular arrays based on the Kirkendall effect and in situ Zn evaporation. *Chem Commun* 30:4548–4550

23. Hossain MM, Mamun AHA, Hahn JR (2012) Fabrication of solid cylindrical-shaped microtowers of ZnO/C core-shell hexagonal nanorods by thermolysis. *J Phys Chem C* 116:23153–23159
24. Paraguay F, Estrada W, Acosta DR, Andrade E, Miki-Yoshida M (1999) Growth, structure and optical characterization of high quality ZnO thin films obtained by spray pyrolysis. *Thin Solid Films* 350:192–202
25. Pol VG, Calderon-Moreno JM, Thiagarajan P (2008) Facile synthesis of novel photoluminescent ZnO micro- and nanowires. *Langmuir* 24:13640–13645
26. Watcharotone S, Dikin DA, Stankovich S, Piner R, Jung I, Dommett GHB, Evmenenko G, Wu SE, Chen SF, Liu CP, Nguyen ST, Ruoff RS (2007) Graphene-silica composite thin films as transparent conductors. *Nano Lett* 7:1888–1892
27. Wang Z-M, Wang WD, Coombs N, Soheilnia N, Ozin GA (2010) Graphene oxide-periodic mesoporous silica sandwich nanocomposites with vertically oriented channels. *ACS Nano* 4:7437–7450
28. Wang HL, Cui LF, Yang Y, Casalongue HS, Robinson JT, Liang YY, Cui Y, Dai HJ (2010) Mn₃O₄-graphene hybrid as a high-capacity anode material for lithium ion batteries. *J Am Chem Soc* 132:13978–13980
29. Son DI, Kwon BW, Park DH, Seo WS, Yi Y, Angadi B, Lee CL, Choi WK (2012) Emissive ZnO-graphene quantum dots for white-light-emitting diodes. *Nat Nanotechnol* 7:465–471
30. Bairamov BH, Heinrich A, Irmer G, Toporov VV, Ziegler E (1983) Raman study of phonon halfwidths and the phonon-plasmon in ZnO. *Phys Status Solidi B* 119:227–234
31. Lv Y, Yu L, Huang H, Feng Y, Chen D, Xie X (2012) Application of the soluble salt-assisted route to scalable synthesis of ZnO nanopowder with repeated photocatalytic activity. *Nanotechnology* 23:065402
32. Salavati-Niasari M, Davar F, Bazarganipour M (2010) Synthesis, characterization and catalytic oxidation of para-xylene by manganese (II) Schiff base complex on functionalized multi-wall carbon nanotubes. *Dalton Trans* 39:7330–7337
33. Teng CC, Ma CCM, Lu CH, Yang SY, Lee SH, Hsiao MC, Yen MY, Chiou KC, Lee TM (2011) Thermal conductivity and structure of non-covalent functionalized graphene/epoxy composites. *Carbon* 49:5107–5116
34. Wang J, Wang Z, Huang B, Ma Y, Liu Y, Qin X, Zhang X, Ying Dai Y (2012) Oxygen vacancy induced band-gap narrowing and enhanced visible light photocatalytic activity of ZnO. *ACS Appl Mater Interfaces* 4:4024–4030
35. Yin X, Hesselink L, Liu Z et al (2004) Large positive and negative lateral optical beam displacements due to surface plasmon resonance. *App Phys Lett* 85:372–374
36. Sherry LJ, Jin R, Mirkin CA et al (2006) Localized surface plasmon resonance spectroscopy of single silver triangular nanoprisms. *Nano Lett* 6:2060–2065
37. Baida H, Billaud P, Marhaba S et al (2009) Quantitative determination of the size dependence of surface plasmon resonance damping in single Ag@ SiO₂ nanoparticles. *Nano Lett* 9:3463–3469
38. Zhang Q, Chou TP, Russo B, Jenekhe SA, Cao G (2008) Poly-disperse aggregates of ZnO nanocrystallites: a method for energy-conversion-efficiency enhancement in dye-sensitized solar cells. *Adv Funct Mater* 18:1654–1660
39. Zhang Q, Chou TP, Russo B, Jenekhe SA, Cao G (2008) Aggregation of ZnO nanocrystallites for high conversion efficiency in dye-sensitized solar cells. *Angew Chem Int Ed* 47:2402–2406
40. Horiuchi H, Katoh R, Hara K, Yanagida M, Murata S, Arakawa H, Tachiya M (2003) Electron injection efficiency from excited N₃ into nanocrystalline ZnO films: effect of (N₃-Zn²⁺) aggregate formation. *J Phys Chem B* 107:2570–2574
41. Shin YJ, Lee JH, Park JH, Park NG (2007) Enhanced photovoltaic properties of SiO₂-treated ZnO nanocrystalline electrode for dye sensitized solar cell. *Chem Lett* 36:1506–1507
42. Law M, Greene LE, Radenovic A, Kuykendall T, Liphardt J, Yang PD (2006) ZnO-Al₂O₃ and ZnO-TiO₂ core-shell nanowire dye-sensitized solar cells. *J Phys Chem B* 110:22652–22663